九州大学学術情報リポジトリ
Kyushu University Institutional Repository

Effect of networked Cu-rich ferrite phase on proof stress and ultimate tensile strength of sintered bodies of Fe-Cu hybrid-alloyed steel powder with graphite

Shigeta, Y.
Department of Materials Physics and Chemistry, Graduate School of Engineering, Kyushu University

Aramaki, Masatoshi
Department of Materials Science and Engineering, Kyushu University

Ashizuka, K.
Steel Research Laboratory, JFE Steel Corporation

Ikoma, Y.
Department of Materials Science and Engineering, Kyushu University

他

https://hdl.handle.net/2324/7183233

出版情報：Powder Metallurgy. 64 (2), pp.134-141, 2021-04-01. Institute of Materials, Minerals and Mining
バージョン：
権利関係：Shigeta Y, Aramaki M, Ashizuka K, Ikoma Y, Ozaki Y. Effect of networked Cu-rich ferrite phase on proof stress and ultimate tensile strength of sintered bodies of Fe-Cu hybrid-alloyed steel powder with graphite. Powder Metallurgy. 2021;64(2):134-141. Copyright © 2021 Institute of Materials, Minerals and Mining Published by Taylor & Francis on behalf of the Institute. DOI:https://doi.org/10.1080/00325899.2021.1871805

KYUSHU UNIVERSITY

Effect of networked Cu-rich ferrite phase on proof stress and ultimate tensile strength of sintered bodies of Fe–Cu hybrid-alloyed steel powder with graphite

To improve the yield strength of PM steel, this work investigated the effect of a Cu-rich networked phase. Mixtures of 0.7% graphite and Fe-3% Cu hybrid-alloyed steel powders, composed of pre-alloyed Fe-3 *x* % Cu particles with diffusion-bonded 3(1- *x*) % Cu ($0 \leq x \leq 1$), were processed by high-density compaction and conventional sintering. The maximum values of 0.2% proof stress (YS) and ultimate tensile strength (UTS) were obtained at $x = 0.68$, where high density compact with well-networked Cu-rich ferrite phase was developed without Cu growth. Moreover, nanosized ε-Cu precipitates were observed in the Cu-rich ferrite. These high YS and UTS were achieved not only by decreases in porosity but also by precipitation strengthening caused by the nanosized ε-Cu in the Cu-rich ferrite network.

Keywords: Cu hybrid alloyed steel powder; proof stress; tensile strength; Cu-rich ferrite network; precipitation strengthening; nanosized ε-Cu precipitates

Introduction

Powder metallurgy (PM) steel is widely used in mechanical and electronic parts because it allows the fabrication of complex-shaped parts at a reasonable cost. However, the mechanical strength of PM steel is lower than that of wrought steels, mainly because pores remain even after compaction and sintering. To minimise the effects of these pores, several kinds of pre-alloyed or partially alloyed steel powders were developed over several decades with the addition of alloying elements such as Ni and Mo [1]. Although high-density compaction and high-alloying systems were developed, the yield strength, toughness, and fatigue strength of such systems are still below those of wrought steel because the remaining pores [2,3] function as stress concentration points. To address the toughness of PM materials, Sekiguchi et al. [4] proposed the development of a ‘harmonic structure’, i.e. coarse matrix grains

surrounded by a networked high-strength fine-grained phase. The harmonic structure could improve both strength and ductility by improving the uniformity of strain distribution, thus delaying localised instability during plastic deformation under load. The well-known Fe–Cu–C system exhibits such a Cu-rich 'harmonic structure'. However, the Cu-rich network is divided by pores remaining after the Cu growth caused by infiltration of the molten Cu during liquid-phase sintering (LPS) [5-20]. The molten Cu is important in LPS, facilitating particle rearrangement and the grain growth of matrix steel powder particles via accelerated diffusion in the liquid phase, which causes the formation of a 'harmonic structure' of networked Cu-rich phase strengthened by fine Cu precipitates. The effect of particle rearrangement, grain growth, and network formation is undermined by the pores remaining in the steel. To eliminate remnant pores in sintered bodies, forging or stamping can be applied. Powder-forged Fe–Cu–C sintered alloys have been applied practically, mainly with PM connecting rods [15-16].

The present study aims to design the above harmonic structure in the Fe–Cu–C system while avoiding Cu growth. To achieve this, high-density compaction and a conventional sintering process using a Fe–3 mass% Cu hybrid-alloyed powder are used. By optimising the volume of molten Cu, Cu growth may be suppressed, thus improving toughness and strength. In this report, the improved proof stress and ultimate tensile strength of the sintered body from the optimised Fe–Cu hybrid-alloyed steel powder are demonstrated.

Experimental procedure

Preparation of Fe–3 mass% Cu hybrid-alloyed steel powder

Pure Fe powder and Fe–0.81 to 3.0 mass% Cu pre-alloyed powders are prepared by water

atomisation. Atomised pure fine Cu powder is mixed with each powder to reach total Cu concentrations reaching 3.0 mass%, followed by diffusion heat treatment. The chemical composition of each hybrid-alloyed steel powder is listed in Table 1. The IDs of the powders are respectively P0, P27, P52, P68, P87, and P100, where the number indicates the ratio of pre-alloyed Cu to the total Cu concentration.

Tensile test and microstructure observations

Each hybrid-alloyed steel powder, mixed with 0.7 mass% natural graphite (average particle size 5 μm), was used to fill a rectangular cavity of 55 mm in length and 10 mm in width by die lubrication with zinc stearate powder. The filled powders were compacted at approximately 1588 MPa, reaching densities of approximately 7.5 Mg/m^3. The green compacts were sintered at 1423 K in a N_2–4 vol.% H_2 gas atmosphere for 1.2 ks. The components of the raw material powders and the green and sintered densities of the specimens are listed in Table 2. The IDs of the sintered specimens are respectively S0, S27, S52, S68, S87, and S100, where the number correspond to those of the raw material powders. The rectangular sintered bodies were machined into specimens for tensile testing with parallel sections measuring 26 mm × 3 mm × 4 mm using a wire-electrical discharge machine. Tensile tests were performed at a strain rate of 3.3×10^{-3} s^{-1}. The strain of each specimen was detected using a strain gauge adhered to the specimen. The microstructures of the sintered bodies were observed with an optical microscope (OM) and a field-emission scanning electron microscope (FE-SEM; Hitachi Co. SU 6600). Cu distribution was evaluated by a field-emission electron probe microanalyzer (EF-EPMA; JEOL Co. JXA 8500F).

Thermal expansion tests

For thermal expansion tests, the mixed powders were combined with 0.5 mass% zinc

stearate powder and compacted into plates of 30 mm × 4 mm × 12 mm with the density of 7.10 Mg/m^3. The longitudinal length of each compact was monitored using a thermomechanical analyser (TMA; Burker Japan TD5,000SA) in N_2–4 vol.% H_2 under heating at 0.1 $K \cdot s^{-1}$, holding at 1423 K for 1.2 ks, and cooling at 0.17 $K \cdot s^{-1}$ to simulate the dimensional change of the specimen during sintering.

Results and discussion

Proof stress, ultimate tensile strength, and sintered density

Each value of the Young's modulus, 0.2% proof stress (noted as YS hereafter), and ultimate tensile stress (UTS) is listed in Table 2. While all powders were compacted to the same green density, the sintered density is also maximised at R_{Cu} = 68%. Since m mechanical properties of sintered materials are usually dependent on their densities, the dependences of the UTS, YS, and Young's modulus on the sintered densities of the specimens are illustrated in Fig. 1. The Young's modulus is almost linearly proportional to the sintered density, as reported in previous works [17-20]. Meanwhile the YS and UTS increased with the sintered density, both showed different dependence trends under and above R_{Cu} = 68%; i.e., the YS and UTS of specimens for which R_{Cu} < 68% are higher than those for which R_{Cu} > 68% at equal densities (Fig. 1(b)). This indicates that the YS and UTS are not determined only by the sintered density in this alloy system. To confirm the strengthened mechanism, work-hardening coefficient, and strength coefficient of each specimen from the true stress–true strain (S–S) curves as shown in Fig.2. The true strain ε_t and the true stress σ_t were obtained from following relations:

$$\sigma_t = \sigma_n(1 + \varepsilon_n), \quad (1)$$

$$\varepsilon_t = \ln(1 + \varepsilon_n), \quad (2)$$

where σ_n is the nominal stress by dividing tensile load by the section area of the unloaded specimen, and ε_n is nominal strain which is calculated by dividing the measured elongation ΔL between the gauge marks by the gauge length L is the distance between the gauge marks. Furthermore, strength coefficient K and work-hardening coefficient n were obtained based on the Hollomon's relation:

$$\sigma_t = K\varepsilon_t^n \quad . \qquad (3)$$

Each dependence of n and K on the sintered densities are shown in Fig.3. As is clear from Fig. 3, n was almost constant regardless of the sintering densities, while K showed the similar density dependence to the YS and UTS. In the condition that n is constant in the Hollomon's relation, the value K can correspond to the yield strength. Therefore, it can be considered the reason why the specimens R_{Cu}<0.68 showed the higher TS than those of R_{Cu}=87 or 100 % at the same density is not due to work-hardening but due to its yield behaviour caused by the material structures. The structural factors that affect the yield strength will be discussed in the following chapters.

Effects of grain size and pore morphology on YS

Figs. 4(a)-4(f) depict OM photographs of all specimens. Ferrite/pearlite structures are observed, and the area of pearlite slightly increased with increased R_{Cu}. Hardness of both phases were measured by a nano-indenter. For example in S68, the hardness of ferrite phase (H_{IT}:3741 N/m^2) was lower than that of the pearlite (H_{IT}:4270 N/m^2) a little. This result indicates that tensile stress may concentrate into ferrite phases between pearlite phases, and its affect the yielding of the specimen. The detail of this point will be mentioned in the next section. The average grain diameter obtained from image analysis, Image-J, are also described above each photo in Fig.4. Firstly, the average grain sizes, which can connect to YS by Balley-Hirsch's relationship, were almost same for all the specimens. Therefore, the effect of

grain size can be excluded from the discussion of YS differences in this case. Second, the pore morphology is changed from a coarse or rough capillary shape to fine and round pores as R_{Cu} increases to 68%. The circularity obtained by image analysis of Figs.4(a)-4(f) increased from 0.88 (S0) up to 0.92 (S68) with increase of R_{Cu}, and it saturated beyond R_{Cu} =68%. The increment in circularity from R_{Cu} =0 to 68 affects to raise the YS and UTS due to suppression of stress concentration.

Fig. 5 shows the dimensional changes estimated from the thermal expansion curves during heating from 1357 K (the melting point of Cu) to 1423 K and holding at 1423 K for 1.2 ks. The former change is positive, so-called Cu growth, and the latter is negative due to sintering shrinkage at the maximum temperature. The behaviour of molten Cu in the Fe–Cu–C system during LPS is well known: it infiltrates fine channels separating powder particles and promotes atomic diffusion between neighbouring steel particles by fast diffusion in the bridging liquid phase, thus resulting in neck growth. As shown in Fig. 5, with increasing R_{Cu}, the Cu growth is decreased, and the sintering shrinkage is decreased significantly in the samples with R_{Cu} = 87 and 100%. Both the decreased Cu growth and sintering shrinkage can be caused by decreases in the volume of molten Cu above 1357 K, i.e. diffusion-bonded Cu. The maximum sintered density at R_{Cu} = 68% is attributed to the minimised Cu growth and sintering shrinkage, compared to those in the specimens at R_{Cu} = 78 or 100%. Meanwhile, the shapes of pores are changed from coarse to fine and round with R_{Cu} increasing to 68%, before becoming rough again in R_{Cu} 78 and 100%. This can be explained by the erosion of rough surfaces of the solid particles and the promoted sintering shrinkage at the maximum temperature. That is, at R_{Cu} = 68%, the spherization and refinement of pores in addition to the minimum porosity contribute to preventing stress concentrations, and thus to the increases in YS.

Effect of Cu distribution

In the previous section, the effects of the grain size and pore morphology on the YS were explained additionally to the density. The other factor to be considered is the Cu distribution. Cu distributions for S0, S27, S52, S68, S87, and S100 obtained from EPMA analysis are respectively depicted in Figs. 6(a)-6(f). Figs. 6(a)-6(e) show a sort of network of Cu-rich area, and the mesh size of the networks seems to become course with increase of the pre-alloyed Cu. This means that the neck growth between Fe–Cu pre-alloyed particles may be promoted with increases in the pre-alloyed Cu content in the γ-particles before Cu melts. From the phase diagram of the Fe–Cu binary system [21], the γ-region, in which Cu diffusion is faster than in the α-phase [22], broadens with increases in Cu content up to 3.06 mass% in the Fe-rich area. The solid-phase diffusion of Cu between pre-alloyed Fe–Cu particles below the melting temperature of Cu can start from lower temperature because the α– γ transformation temperature decreases with increases in the pre-alloyed Cu content. As a result, such Cu diffusion promotes neck growth forming coarse network of channels where Cu melt infilters during the LPS. Based on the line analysis of Cu concentration along the lines depicted in Figs.6(a)-6(f), both Cu concentrations in the Cu-rich area and the Cu-dilute area are plotted in Figs.7(a) and 7(b). It should be mentioned that the difference is R_{Cu}<68%.

For specimen S68, the Cu distribution map and the OM image in the same field of view are shown in Fig. 8. Almost all pearlite grains correspond to Cu-dilute areas inside the Cu-rich network, i.e. almost all of the Cu-rich mesh phase may be ferrite. From Fig 7, Cu concentrations in the Cu-rich network of R_{Cu}<68% are much higher than those of R_{Cu}>68%. Chen et al. estimated the effect of C addition to Fe–Cu by using CALPHAD at 1123 K. In the area with >3 mass% Cu and C ≤ 0.70 mass%, αFe + εCu is stable. Therefore, in the nanoprecipitates are considered as ε-Cu precipitates formed during

cooling. In the Cu rich network, such ε-Cu nano-precipitates in Cu-rich ferrite in the Fe–Cu–C system have been investigated in both hot-rolled steel [23] and sintered bodies [24]. In the specimens R_{Cu}<68%, it is considered that nano-ε-Cu can precipitate in the Cu-rich network where Cu is concentrated more than 3 mass%. Nano-sized precipitates are observed in the magnified SEM image of the Cu-rich ferrite mesh near a pearlite region, as shown inside the dashed circle in Fig. 9. Furthermore, about 10 nm of coherent precipitates with body centred cubic (bcc) structure were observed in α-Fe matrix in the Cu-rich area of S68 by high resolution transmission electron microscopy (HRTEM) observation. This is supported by several recent researches, e.c., the precipitation of 3–5 nm-sized bcc Cu in ferrite matrix during aging of Fe–3Si–2Cu in was confirmed by high-angle annular dark-field scanning transmission electron microscopy imaging [25]. More details will be reported in our future work. Such coherent nano-Cu-precipitates can be pinning site of dislocations during elastic deformation resulting in delaying the share slip.

As shown in Fig. 3(a), under R_{Cu} = 68% where the Cu-rich network structures are observed, the YS is higher than those beyond R_{Cu} = 68%. The Cu-rich α-network can affect the YS by homogeneously distributing stress applied to the specimen in the Cu-rich α-network. Once the elastic strain is dispersed in the Cu-rich α-network, the dislocations can be pinned at the nano-precipitates of Cu. This estimation is supported by the remarkable work-hardening observed in the S–S curve of the S68 specimen. For a Cu-rich network divided by pores, like those observed in S0, S27, and S52, the stress can become locally concentrated around these pores. As Cu concentrations in ferrite phase decrease less than the other specimens in S87 or S100, the number of Cu precipitates may decrease. In both cases, dislocation pinning by Cu nano-precipitates cannot be expected.

In conclusion, the YS can be improved by the Cu-rich α-network with fewer pores, i.e., the Cu-rich network structure.

Conclusions

A harmonic structure within a PM steel specimen was designed for a sintered Fe–3 mass% Cu–0.7 mass% C system using Fe–3 mass% Cu hybrid-alloyed steel powder by high-pressure compaction and conventional sintering. The optimised hybrid-alloyed steel powder was formed with Fe-2.04 mass% Cu pre-alloyed steel powder particles that were diffusion-bonded with 0.96 mass% pure Cu, such that the ratio of pre-alloyed Cu of the total Cu content, R_{Cu}, was 68%. Using the optimised powder, the YS and UTS of the sintered body reached 533 MPa and 758 MPa, respectively. These properties at the optimum composition may arise from the following mechanisms:

(1) The maximum sintered density of 7.56 Mg/m^3 was achieved by reduced Cu growth and shrinkage at the highest sintering temperature, induced by the optimisation of Cu liquid phase during liquid-phase sintering (LPS).

(2) At the maximum sintered density, the Young's modulus, YS, and UTS were maximised because the number of pores as stress concentration sites was reduced. The Young's modulus was linearly proportional to the sintered density, as explained in previous studies. However, at the same density, the YS and UTS of the specimens obtained via LPS with the optimum liquid

phase were higher than those of the specimens sintered with less or no liquid phase.

(3) Density dependences of the YS and UTS can be well connected to Strength coefficient obtained from Hollow's relation, which corresponds to Yield behaviour of materials.

(4) A Cu-rich ferrite (α) mesh that was well-networked without division by pores, was formed around pearlite grains in the specimen. The well-networked Cu-rich α-mesh may disperse stress uniformly and thus delay localised share slip during elastic deformation.

(5) In the well-networked Cu-rich α-mesh nano-sized precipitates, which can be ε-Cu, were observed; these would induce work-strengthening under tensile stress during elastic deformation.

From the above, the improved values of YS and UTS can be achieved by suppressing the strain concentration and increasing yielding point by establishing the Cu-rich α-network with precipitation strengthening by nano-sized Cu precipitates. It is expected in the future that the strength can be further improved by controlling the cooling rate, which affects the cementite formation and the number density and size of precipitates in the Cu-rich α-network.

References

[1] Lindskog P. The history of Distaloy. Powder Metall. 2013;56(5):351–361.

[2] Unami S, Ozaki Y, Ushirosako T, Tanino H. Development of molybdenum hybrid-alloyed steel powder for high fatigue strength sintered parts. Jap J Powder Metall. 2010;57(5):341–347.

[3] Dlapka M, Danninger H, Gierl C, Lindqvist B. Defining the pores in PM components. Metal Powder Report 2010;65(2):30–33. https://doi.org/10.1016/S0026-0657(10)70093-X.

[4] Sekiguchi S, Ono K, Fujiwara J, Ameyama K. New microstructure design for commercially pure Titanium with outstanding mechanical properties by mechanical milling and hot roll sintering. Mater Trans. 2010;51(1):39–45. https://doi.org/10.2320/matertrans.MB200913.

[5] Tahir AM, Amberg G, Hedström P, Bergman O, Frisk K. Cu redistribution during sintering of Fe–2Cu and Fe–2Cu–0·5C compacts. Powder Metall. 2014;57(5):373–379.

[6] Bocksteigel, G. Erscheinungsbild und ursachen von volumenanderungen beim sintern von presslingen aus eisen-kupfer- und eisen-kupfer-graphit-pulvermischungen [Appearance and causes of changes in volume when sintering compacts from iron-copper and iron-copper-graphite powder mixtures]. Stahl Eisen. 1959;79(8):1187–1201.

[7] Durdaller D. Technical bulletin from Höanäs Corporation, 174D(1971) 471.

[8] Findeisen G. Einige mit Kupfer und Nickel Legierte Sinterstaehle: Inre eigenschaten und herstellung [Some sintered steels alloyed with copper and nickel: their properties and manufacture]. Metall. 1960;14:295.

[9] Jamil S-J, Chadwick G-A. Investigation and analysis of liquid phase sintering of Fe-Cu and Fe-Cu-C compacts. Powder Metall. 1958;28(2):65–71.

[10] Krantz T. Effect of density and composition on the dimensional stability and strength of iron-copper alloys. Int J Powder Metall. 1969;5(3):35–43.

[11] Lawcock R-L, Davies T-J. Effect of carbon on dimensional and microstructural characteristics of Fe–Cu compacts during sintering. Powder Metall. 1990;33(2):147–150.

[12] Angers R, Trudel Y. Modern development in powder metallurgy. Vol. 6, Applications and Processes. Princeton, N-J: Metal Powder Industries Federation; 1974.

[13] Danninger H. Sintering of Mo alloyed P/M steels prepared from elemental powders. II: Mo homogenization and dimensional behaviour. Powder Metall Int. 1992;24(3):163–168.

[14] Danninger H , Kara T. Influence of manufacturing parameters on the sintering of Mo alloyed structural steels. Powder Metall Int. 1988;20(12):9–13.

[15] Fischmeister H-F, Larsson L-E. Fast diffusion alloying for powder forging using a liquid phase. Powder Metall. 1974;17(33):227–240.

[16] Dogan B, Davies T-J. Controlled rolled low alloy powder forged steels. Powder Metall. 1985;28(4):225–230.

[17] Phani K-K, Niyogi S-K. Young's modulus of porous materials. J Mater Sci. 1987;22(1):257–263.

[18] Wang JC. Young's modulus of porous materials. II: Young's modulus of porous alumina with changing pore structure. J Mater Sci. 1984;19(3):809–814.

[19] Hasselman D-P-H. Relation between effects of porosity on strength and on Young's modulus of elasticity of polycrystalline materials. Amer Cer Soc. 1962;46(11):564–565. https://doi.org/10.1111/j.1151-2916.1963.tb14615.x

[20] Miura H, Sakamoto A, Tokunaga Y. Effect of porosity and pore shape on the Young’s moduli of sintered iron and steel. Jap J Powder Metall. 1980;27(3):82–87.

[21] Chen L, Zhang Z, Haung Y, Cui J, Deng Z, Zou H, Chang K. Thermodynamic description of the Fe–Cu–C system. CALPHAD 2019;64:225–235.

[22] Rothmoan S-J, Peterson N-L, Walter C-M, Nowicki L-J. The diffusion of copper in Iron. J Appl Phys. 1968;39: 5041–5044.

[23] Ilia E, Plamondon P, Masse J-P, L'Espérance G. Copper precipitation at engine operating temperatures in powder-forged connecting rods manufactured with Fe–Cu–C alloys. Mater Sci Eng A. 2019;767(8):138383–138391.

[24] Othen P-J, Jenkins M-L, Smith G-D-W. High-resolution electron microscopy studies of the structure of Cu precipitates in α-Fe. Philos Mag. 1994;70A:1–24.

[25] Heo Y-U, Kim Y-K, Kim J-S, Kim J-K. Phase transformation of Cu precipitates from bcc to fcc in Fe–3Si–2Cu alloy. Acta Material. 2013;61: 519–528.

Table 1. Chemical composition designed for Fe–3 mass% Cu hybrid alloyed steel powders.

Powder ID	Pre-alloyed Fe-Cu powder		Diffusion-bonded Cu (mass%)	Pre-alloyed Cu ratio R_{Cu} (%)	Diffusion-bonded Cu ratio (%)
	Cu (mass%)	Fe (mass%)			
P0	0.00	bal.	3.0	0	100
P27	0.80	bal.	2.2	27	87
P52	1.60	bal.	1.4	52	68
P68	2.00	bal.	1.0	68	52
P87	2.60	bal.	0.4	87	27
P100	3.00	bal.	0.0	100	0

Table 2. Components of raw material mixed powders, green density, and mechanical properties of sintered bodies.

Sintered specimen ID	Raw material powder mixture		Green density (Mg/m^3)	Properties of sintered bodies			
	Hybrid alloyed powder	Graphite powder (mass%)		Sintered density (Mg/m^3)	Young's modulus (GPa)	0.2% Proof stress YS (MPa)	UTS (MPa)
S0	P0	0.70	7.50	7.47	165	449	653
S27	P27	0.70	7.50	7.48	164	464	663
S52	P52	0.70	7.49	7.50	168	493	678
S68	P68	0.70	7.50	7.56	170	517	726
S87	P87	0.70	7.52	7.55	171	486	654
S100	P100	0.70	7.52	7.54	170	468	661

Figure 1. (a) Strength and (b) Young's modulus vs. sintered density of Fe-3 mass% Cu hybrid steel alloyed powder + 0.7 mass% C. Number for each datapoint indicates R_{Cu}.

Figure 2. True stress-true strain curves of the sintered bodies, S0, S27, S52, S68, S87 and S100.

Figure 3. (a) Work hardening coefficient, n and (b) Strength Coefficient, K of sintered bodies vs. sintered density of Fe-3 mass% Cu hybrid steel alloyed powder + 0.7 mass% C. Number for each datapoint indicates R_{Cu}.

Figure 4. Optical microscopic images of the sintered specimens: (a) S0, (b) S27, (c) S52, (d) S68, (e) S87, and (f) S100, where d shows average grain diameter.

Figure 5. Dimensional changes vs. pre-alloyed Cu ratio in the Fe-3 mass% Cu hybrid steel alloyed powder.

Figure 6. Maps of Cu distribution obtained by EMPA for the sintered specimens: (a) S0, (b) S27, (c) S52, (d) S68, (e) S87, and (f) S100. White profile in each map illustrates the Cu concentration along the white line.

Figure 7. Average Cu concentrations of Cu-rich Cu-dilute areas estimated from the line analyses of Cu concentration shown in Figs.6(a)-6(f).

Figure 8. Comparison between the map of Cu distribution (left) and the optical micrograph (right) of S68 in the same field of view.

Figure 9. Nano-sized precipitates in ferrite phase surrounding pearlite phase, observed in specimen S68.

Manuscript (NOT PDF FILE AT REVISE STAGE)
Click here to access/download;Manuscript (NOT PDF FILE AT REVISE STAGE);MS_Yukiko Ozaki_Revised_201226.docx

Effect of networked Cu-rich ferrite phase on proof stress and ultimate tensile strength of sintered bodies of Fe–Cu hybrid-alloyed steel powder with graphite

Y. Shigeta[b], M. Aramaki[a] , K. Ashizuka[c], Y. Ikoma[a] and Y. Ozaki[a]*

[a] *Department of Materials Science and Engineering, Kyushu University, 744, Motooka, Nishi-ku, Fukuoka 819-0395, Japan;* [b] *Department of Materials Physics and Chemistry, Graduate School of Engineering, Kyushu University, 744, Motooka, Nishi-ku, Fukuoka 819-0395, Japan;* [c] *Steel Research Laboratory, JFE Steel Corporation, Chiba 260-0835, Japan*

*Corresponding author: Department of Materials Science and Engineering, Kyushu University, 744, Motooka, Nishi-ku, Fukuoka 819-0395, Japan. E-mail address: ozaki@zaiko.kyushu-u.ac.jp

Effect of networked Cu-rich ferrite phase on proof stress and ultimate tensile strength of sintered bodies of Fe–Cu hybrid-alloyed steel powder with graphite

To improve the yield strength of PM steel, this work investigated the effect of a Cu-rich networked phase. Mixtures of 0.7% graphite and Fe-3% Cu hybrid-alloyed steel powders, composed of pre-alloyed Fe-3 *x* % Cu particles with diffusion-bonded 3(1- *x*) % Cu ($0 \leq x \leq 1$), were processed by high-density compaction and conventional sintering. The maximum values of 0.2% proof stress (YS) and ultimate tensile strength (UTS) were obtained at $x = 0.68$, where high density compact with well-networked Cu-rich ferrite phase was developed without Cu growth. Moreover, nanosized ε-Cu precipitates were observed in the Cu-rich ferrite. These high YS and UTS were achieved not only by decreases in porosity but also by precipitation strengthening caused by the nanosized ε-Cu in the Cu-rich ferrite network.

Keywords: Cu hybrid alloyed steel powder; proof stress; tensile strength; Cu-rich ferrite network; precipitation strengthening; nanosized ε-Cu precipitates

Introduction

Powder metallurgy (PM) steel is widely used in mechanical and electronic parts because it allows the fabrication of complex-shaped parts at a reasonable cost. However, the mechanical strength of PM steel is lower than that of wrought steels, mainly because pores remain even after compaction and sintering. To minimise the effects of these pores, several kinds of pre-alloyed or partially alloyed steel powders were developed over several decades with the addition of alloying elements such as Ni and Mo [1]. Although high-density compaction and high-alloying systems were developed, the yield strength, toughness, and fatigue strength of such systems are still below those of wrought steel because the remaining pores [2,3] function as stress concentration points. To address the toughness of PM materials, Sekiguchi et al. [4] proposed the development of a ‘harmonic structure’, i.e. coarse matrix grains

surrounded by a networked high-strength fine-grained phase. The harmonic structure could improve both strength and ductility by improving the uniformity of strain distribution, thus delaying localised instability during plastic deformation under load. The well-known Fe–Cu–C system exhibits such a Cu-rich 'harmonic structure'. However, the Cu-rich network is divided by pores remaining after the Cu growth caused by infiltration of the molten Cu during liquid-phase sintering (LPS) [5-20]. The molten Cu is important in LPS, facilitating particle rearrangement and the grain growth of matrix steel powder particles via accelerated diffusion in the liquid phase, which causes the formation of a 'harmonic structure' of networked Cu-rich phase strengthened by fine Cu precipitates. The effect of particle rearrangement, grain growth, and network formation is undermined by the pores remaining in the steel. To eliminate remnant pores in sintered bodies, forging or stamping can be applied. Powder-forged Fe–Cu–C sintered alloys have been applied practically, mainly with PM connecting rods [15-16].

The present study aims to design the above harmonic structure in the Fe–Cu–C system while avoiding Cu growth. To achieve this, high-density compaction and a conventional sintering process using a Fe–3 mass% Cu hybrid-alloyed powder are used. By optimising the volume of molten Cu, Cu growth may be suppressed, thus improving toughness and strength. In this report, the improved proof stress and ultimate tensile strength of the sintered body from the optimised Fe–Cu hybrid-alloyed steel powder are demonstrated.

Experimental procedure

Preparation of Fe–3 mass% Cu hybrid-alloyed steel powder

Pure Fe powder and Fe–0.81 to 3.0 mass% Cu pre-alloyed powders are prepared by water

atomisation. Atomised pure fine Cu powder is mixed with each powder to reach total Cu concentrations reaching 3.0 mass%, followed by diffusion heat treatment. The chemical composition of each hybrid-alloyed steel powder is listed in Table 1. The IDs of the powders are respectively P0, P27, P52, P68, P87, and P100, where the number indicates the ratio of pre-alloyed Cu to the total Cu concentration.

Tensile test and microstructure observations

Each hybrid-alloyed steel powder, mixed with 0.7 mass% natural graphite (average particle size 5 μm), was used to fill a rectangular cavity of 55 mm in length and 10 mm in width by die lubrication with zinc stearate powder. The filled powders were compacted at approximately 1588 MPa, reaching densities of approximately 7.5 Mg/m^3. The green compacts were sintered at 1423 K in a N_2–4 vol.% H_2 gas atmosphere for 1.2 ks. The components of the raw material powders and the green and sintered densities of the specimens are listed in Table 2. The IDs of the sintered specimens are respectively S0, S27, S52, S68, S87, and S100, where the number correspond to those of the raw material powders. The rectangular sintered bodies were machined into specimens for tensile testing with parallel sections measuring 26 mm × 3 mm × 4 mm using a wire-electrical discharge machine. Tensile tests were performed at a strain rate of 3.3×10^{-3} s^{-1}. The strain of each specimen was detected using a strain gauge adhered to the specimen. The microstructures of the sintered bodies were observed with an optical microscope (OM) and a field-emission scanning electron microscope (FE-SEM; Hitachi Co. SU 6600). Cu distribution was evaluated by a field-emission electron probe microanalyzer (EF-EPMA; JEOL Co. JXA 8500F).

Thermal expansion tests

For thermal expansion tests, the mixed powders were combined with 0.5 mass% zinc

stearate powder and compacted into plates of 30 mm × 4 mm × 12 mm with the density of 7.10 Mg/m^3. The longitudinal length of each compact was monitored using a thermomechanical analyser (TMA; Burker Japan TD5,000SA) in N_2–4 vol.% H_2 under heating at 0.1 $K \cdot s^{-1}$, holding at 1423 K for 1.2 ks, and cooling at 0.17 $K \cdot s^{-1}$ to simulate the dimensional change of the specimen during sintering.

Results and discussion

Proof stress, ultimate tensile strength, and sintered density

Each value of the Young's modulus, 0.2% proof stress (noted as YS hereafter), and ultimate tensile stress (UTS) is listed in Table 2. While all powders were compacted to the same green density, the sintered density is also maximised at R_{Cu} = 68%. Since m mechanical properties of sintered materials are usually dependent on their densities, the dependences of the UTS, YS, and Young's modulus on the sintered densities of the specimens are illustrated in Fig. 1. The Young's modulus is almost linearly proportional to the sintered density, as reported in previous works [17-20]. Meanwhile the YS and UTS increased with the sintered density, both showed different dependence trends under and above R_{Cu} = 68%; i.e., the YS and UTS of specimens for which R_{Cu} < 68% are higher than those for which R_{Cu} > 68% at equal densities (Fig. 1(b)). This indicates that the YS and UTS are not determined only by the sintered density in this alloy system. To confirm the strengthened mechanism, work-hardening coefficient, and strength coefficient of each specimen from the true stress–true strain (S–S) curves as shown in Fig.2. The true strain ε_t and the true stress σ_t were obtained from following relations:

$$\sigma_t = \sigma_n(1 + \varepsilon_n), \quad (1)$$

$$\varepsilon_t = \ln(1 + \varepsilon_n), \quad (2)$$

where σ_n is the nominal stress by dividing tensile load by the section area of the unloaded specimen, and ε_n is nominal strain which is calculated by dividing the measured elongation ΔL between the gauge marks by the gauge length L is the distance between the gauge marks. Furthermore, strength coefficient K and work-hardening coefficient n were obtained based on the Hollomon's relation:

$$\sigma_t = K\varepsilon_t^n \quad . \qquad (3)$$

Each dependence of n and K on the sintered densities are shown in Fig.3. As is clear from Fig. 3, n was almost constant regardless of the sintering densities, while K showed the similar density dependence to the YS and UTS. In the condition that n is constant in the Hollomon's relation, the value K can correspond to the yield strength. Therefore, it can be considered the reason why the specimens R_{Cu}<0.68 showed the higher TS than those of R_{Cu}=87 or 100 % at the same density is not due to work-hardening but due to its yield behaviour caused by the material structures. The structural factors that affect the yield strength will be discussed in the following chapters.

Effects of grain size and pore morphology on YS

Figs. 4(a)-4(f) depict OM photographs of all specimens. Ferrite/pearlite structures are observed, and the area of pearlite slightly increased with increased R_{Cu}. Hardness of both phases were measured by a nano-indenter. For example in S68, the hardness of ferrite phase (H_{IT}:3741 N/m^2) was lower than that of the pearlite (H_{IT}:4270 N/m^2) a little. This result indicates that tensile stress may concentrate into ferrite phases between pearlite phases, and its affect the yielding of the specimen. The detail of this point will be mentioned in the next section. The average grain diameter obtained from image analysis, Image-J, are also described above each photo in Fig.4. Firstly, the average grain sizes, which can connect to YS by Balley-Hirsch's relationship, were almost same for all the specimens. Therefore, the effect of

grain size can be excluded from the discussion of YS differences in this case. Second, the pore morphology is changed from a coarse or rough capillary shape to fine and round pores as R_{Cu} increases to 68%. The circularity obtained by image analysis of Figs.4(a)-4(f) increased from 0.88 (S0) up to 0.92 (S68) with increase of R_{Cu}, and it saturated beyond R_{Cu} =68%. The increment in circularity from R_{Cu} =0 to 68 affects to raise the YS and UTS due to suppression of stress concentration.

Fig. 5 shows the dimensional changes estimated from the thermal expansion curves during heating from 1357 K (the melting point of Cu) to 1423 K and holding at 1423 K for 1.2 ks. The former change is positive, so-called Cu growth, and the latter is negative due to sintering shrinkage at the maximum temperature. The behaviour of molten Cu in the Fe–Cu–C system during LPS is well known: it infiltrates fine channels separating powder particles and promotes atomic diffusion between neighbouring steel particles by fast diffusion in the bridging liquid phase, thus resulting in neck growth. As shown in Fig. 5, with increasing R_{Cu}, the Cu growth is decreased, and the sintering shrinkage is decreased significantly in the samples with R_{Cu} = 87 and 100%. Both the decreased Cu growth and sintering shrinkage can be caused by decreases in the volume of molten Cu above 1357 K, i.e. diffusion-bonded Cu. The maximum sintered density at R_{Cu} = 68% is attributed to the minimised Cu growth and sintering shrinkage, compared to those in the specimens at R_{Cu} = 78 or 100%. Meanwhile, the shapes of pores are changed from coarse to fine and round with R_{Cu} increasing to 68%, before becoming rough again in R_{Cu} 78 and 100%. This can be explained by the erosion of rough surfaces of the solid particles and the promoted sintering shrinkage at the maximum temperature. That is, at R_{Cu} = 68%, the spherization and refinement of pores in addition to the minimum porosity contribute to preventing stress concentrations, and thus to the increases in YS.

Effect of Cu distribution

In the previous section, the effects of the grain size and pore morphology on the YS were explained additionally to the density. The other factor to be considered is the Cu distribution. Cu distributions for S0, S27, S52, S68, S87, and S100 obtained from EPMA analysis are respectively depicted in Figs. 6(a)-6(f). Figs. 6(a)-6(e) show a sort of network of Cu-rich area, and the mesh size of the networks seems to become course with increase of the pre-alloyed Cu. This means that the neck growth between Fe–Cu pre-alloyed particles may be promoted with increases in the pre-alloyed Cu content in the γ-particles before Cu melts. From the phase diagram of the Fe–Cu binary system [21], the γ-region, in which Cu diffusion is faster than in the α-phase [22], broadens with increases in Cu content up to 3.06 mass% in the Fe-rich area. The solid-phase diffusion of Cu between pre-alloyed Fe–Cu particles below the melting temperature of Cu can start from lower temperature because the α– γ transformation temperature decreases with increases in the pre-alloyed Cu content. As a result, such Cu diffusion promotes neck growth forming coarse network of channels where Cu melt infilters during the LPS. Based on the line analysis of Cu concentration along the lines depicted in Figs.6(a)-6(f), both Cu concentrations in the Cu-rich area and the Cu-dilute area are plotted in Figs.7(a) and 7(b). It should be mentioned that the difference is R_{Cu}<68%.

For specimen S68, the Cu distribution map and the OM image in the same field of view are shown in Fig. 8. Almost all pearlite grains correspond to Cu-dilute areas inside the Cu-rich network, i.e. almost all of the Cu-rich mesh phase may be ferrite. From Fig 7, Cu concentrations in the Cu-rich network of R_{Cu}<68% are much higher than those of R_{Cu}>68%. Chen et al. estimated the effect of C addition to Fe–Cu by using CALPHAD at 1123 K. In the area with >3 mass% Cu and C ≤ 0.70 mass%, αFe + εCu is stable. Therefore, in the nanoprecipitates are considered as ε-Cu precipitates formed during

cooling. In the Cu rich network, such ε-Cu nano-precipitates in Cu-rich ferrite in the Fe–Cu–C system have been investigated in both hot-rolled steel [23] and sintered bodies [24]. In the specimens R_{Cu}<68%, it is considered that nano-ε-Cu can precipitate in the Cu-rich network where Cu is concentrated more than 3 mass%. Nano-sized precipitates are observed in the magnified SEM image of the Cu-rich ferrite mesh near a pearlite region, as shown inside the dashed circle in Fig. 9. Furthermore, about 10 nm of coherent precipitates with body centred cubic (bcc) structure were observed in α-Fe matrix in the Cu-rich area of S68 by high resolution transmission electron microscopy (HRTEM) observation. This is supported by several recent researches, e.c., the precipitation of 3–5 nm-sized bcc Cu in ferrite matrix during aging of Fe–3Si–2Cu in was confirmed by high-angle annular dark-field scanning transmission electron microscopy imaging [25]. More details will be reported in our future work. Such coherent nano-Cu-precipitates can be pinning site of dislocations during elastic deformation resulting in delaying the share slip.

As shown in Fig. 3(a), under R_{Cu} = 68% where the Cu-rich network structures are observed, the YS is higher than those beyond R_{Cu} = 68%. The Cu-rich α-network can affect the YS by homogeneously distributing stress applied to the specimen in the Cu-rich α-network. Once the elastic strain is dispersed in the Cu-rich α-network, the dislocations can be pinned at the nano-precipitates of Cu. This estimation is supported by the remarkable work-hardening observed in the S–S curve of the S68 specimen. For a Cu-rich network divided by pores, like those observed in S0, S27, and S52, the stress can become locally concentrated around these pores. As Cu concentrations in ferrite phase decrease less than the other specimens in S87 or S100, the number of Cu precipitates may decrease. In both cases, dislocation pinning by Cu nano-precipitates cannot be expected.

In conclusion, the YS can be improved by the Cu-rich α-network with fewer pores, i.e., the Cu-rich network structure.

Conclusions

A harmonic structure within a PM steel specimen was designed for a sintered Fe–3 mass% Cu–0.7 mass% C system using Fe–3 mass% Cu hybrid-alloyed steel powder by high-pressure compaction and conventional sintering. The optimised hybrid-alloyed steel powder was formed with Fe-2.04 mass% Cu pre-alloyed steel powder particles that were diffusion-bonded with 0.96 mass% pure Cu, such that the ratio of pre-alloyed Cu of the total Cu content, R_{Cu}, was 68%. Using the optimised powder, the YS and UTS of the sintered body reached 533 MPa and 758 MPa, respectively. These properties at the optimum composition may arise from the following mechanisms:

(1) The maximum sintered density of 7.56 Mg/m^3 was achieved by reduced Cu growth and shrinkage at the highest sintering temperature, induced by the optimisation of Cu liquid phase during liquid-phase sintering (LPS).

(2) At the maximum sintered density, the Young's modulus, YS, and UTS were maximised because the number of pores as stress concentration sites was reduced. The Young's modulus was linearly proportional to the sintered density, as explained in previous studies. However, at the same density, the YS and UTS of the specimens obtained via LPS with the optimum liquid

phase were higher than those of the specimens sintered with less or no liquid phase.

(3) Density dependences of the YS and UTS can be well connected to Strength coefficient obtained from Hollow's relation, which corresponds to Yield behaviour of materials.

(4) A Cu-rich ferrite (α) mesh that was well-networked without division by pores, was formed around pearlite grains in the specimen. The well-networked Cu-rich α-mesh may disperse stress uniformly and thus delay localised share slip during elastic deformation.

(5) In the well-networked Cu-rich α-mesh nano-sized precipitates, which can be ε-Cu, were observed; these would induce work-strengthening under tensile stress during elastic deformation.

From the above, the improved values of YS and UTS can be achieved by suppressing the strain concentration and increasing yielding point by establishing the Cu-rich α-network with precipitation strengthening by nano-sized Cu precipitates. It is expected in the future that the strength can be further improved by controlling the cooling rate, which affects the cementite formation and the number density and size of precipitates in the Cu-rich α-network.

References

[1] Lindskog P. The history of Distaloy. Powder Metall. 2013;56(5):351–361.

[2] Unami S, Ozaki Y, Ushirosako T, Tanino H. Development of molybdenum hybrid-alloyed steel powder for high fatigue strength sintered parts. Jap J Powder Metall. 2010;57(5):341–347.

[3] Dlapka M, Danninger H, Gierl C, Lindqvist B. Defining the pores in PM components. Metal Powder Report 2010;65(2):30–33. https://doi.org/10.1016/S0026-0657(10)70093-X.

[4] Sekiguchi S, Ono K, Fujiwara J, Ameyama K. New microstructure design for commercially pure Titanium with outstanding mechanical properties by mechanical milling and hot roll sintering. Mater Trans. 2010;51(1):39–45. https://doi.org/10.2320/matertrans.MB200913.

[5] Tahir AM, Amberg G, Hedström P, Bergman O, Frisk K. Cu redistribution during sintering of Fe–2Cu and Fe–2Cu–0·5C compacts. Powder Metall. 2014;57(5):373–379.

[6] Bocksteigel, G. Erscheinungsbild und ursachen von volumenanderungen beim sintern von presslingen aus eisen-kupfer- und eisen-kupfer-graphit-pulvermischungen [Appearance and causes of changes in volume when sintering compacts from iron-copper and iron-copper-graphite powder mixtures]. Stahl Eisen. 1959;79(8):1187–1201.

[7] Durdaller D. Technical bulletin from Höanäs Corporation, 174D(1971) 471.

[8] Findeisen G. Einige mit Kupfer und Nickel Legierte Sinterstaehle: Inre eigenschaten und herstellung [Some sintered steels alloyed with copper and nickel: their properties and manufacture]. Metall. 1960;14:295.

[9] Jamil S-J, Chadwick G-A. Investigation and analysis of liquid phase sintering of Fe-Cu and Fe-Cu-C compacts. Powder Metall. 1958;28(2):65–71.

[10] Krantz T. Effect of density and composition on the dimensional stability and strength of iron-copper alloys. Int J Powder Metall. 1969;5(3):35–43.

[11] Lawcock R-L, Davies T-J. Effect of carbon on dimensional and microstructural characteristics of Fe–Cu compacts during sintering. Powder Metall. 1990;33(2):147–150.

[12] Angers R, Trudel Y. Modern development in powder metallurgy. Vol. 6, Applications and Processes. Princeton, N-J: Metal Powder Industries Federation; 1974.

[13] Danninger H. Sintering of Mo alloyed P/M steels prepared from elemental powders. II: Mo homogenization and dimensional behaviour. Powder Metall Int. 1992;24(3):163–168.

[14] Danninger H , Kara T. Influence of manufacturing parameters on the sintering of Mo alloyed structural steels. Powder Metall Int. 1988;20(12):9–13.

[15] Fischmeister H-F, Larsson L-E. Fast diffusion alloying for powder forging using a liquid phase. Powder Metall. 1974;17(33):227–240.

[16] Dogan B, Davies T-J. Controlled rolled low alloy powder forged steels. Powder Metall. 1985;28(4):225–230.

[17] Phani K-K, Niyogi S-K. Young's modulus of porous materials. J Mater Sci. 1987;22(1):257–263.

[18] Wang JC. Young's modulus of porous materials. II: Young's modulus of porous alumina with changing pore structure. J Mater Sci. 1984;19(3):809–814.

[19] Hasselman D-P-H. Relation between effects of porosity on strength and on Young's modulus of elasticity of polycrystalline materials. Amer Cer Soc. 1962;46(11):564–565. https://doi.org/10.1111/j.1151-2916.1963.tb14615.x

[20] Miura H, Sakamoto A, Tokunaga Y. Effect of porosity and pore shape on the Young’s moduli of sintered iron and steel. Jap J Powder Metall. 1980;27(3):82–87.

[21] Chen L, Zhang Z, Haung Y, Cui J, Deng Z, Zou H, Chang K. Thermodynamic description of the Fe–Cu–C system. CALPHAD 2019;64: 225–235.

[22] Rothmoan S-J, Peterson N-L, Walter C-M, Nowicki L-J. The diffusion of copper in Iron. J Appl Phys. 1968;39: 5041–5044.

[23] Ilia E, Plamondon P, Masse J-P, L'Espérance G. Copper precipitation at engine operating temperatures in powder-forged connecting rods manufactured with Fe–Cu–C alloys. Mater Sci Eng A. 2019;767(8):138383–138391.

[24] Othen P-J, Jenkins M-L, Smith G-D-W. High-resolution electron microscopy studies of the structure of Cu precipitates in α-Fe. Philos Mag. 1994;70A:1–24.

[25] Heo Y-U, Kim Y-K, Kim J-S, Kim J-K. Phase transformation of Cu precipitates from bcc to fcc in Fe–3Si–2Cu alloy. Acta Material. 2013;61: 519–528.

Table 1. Chemical composition designed for Fe–3 mass% Cu hybrid alloyed steel powders.

Powder ID	Pre-alloyed Fe-Cu powder		Diffusion-bonded Cu (mass%)	Pre-alloyed Cu ratio R_{Cu} (%)	Diffusion-bonded Cu ratio (%)
	Cu (mass%)	Fe (mass%)			
P0	0.00	bal.	3.0	0	100
P27	0.80	bal.	2.2	27	87
P52	1.60	bal.	1.4	52	68
P68	2.00	bal.	1.0	68	52
P87	2.60	bal.	0.4	87	27
P100	3.00	bal.	0.0	100	0

Table 2. Components of raw material mixed powders, green density, and mechanical properties of sintered bodies.

Sintered specimen ID	Raw material powder mixture		Green density (Mg/m^3)	Properties of sintered bodies			
	Hybrid alloyed powder	Graphite powder (mass%)		Sintered density (Mg/m^3)	Young's modulus (GPa)	0.2% Proof stress YS (MPa)	UTS (MPa)
S0	P0	0.70	7.50	7.47	165	449	653
S27	P27	0.70	7.50	7.48	164	464	663
S52	P52	0.70	7.49	7.50	168	493	678
S68	P68	0.70	7.50	7.56	170	517	726
S87	P87	0.70	7.52	7.55	171	486	654
S100	P100	0.70	7.52	7.54	170	468	661

Figure 1. (a) Strength and (b) Young's modulus vs. sintered density of Fe-3 mass% Cu hybrid steel alloyed powder + 0.7 mass% C. Number for each datapoint indicates R_{Cu}.

Figure 2. True stress-true strain curves of the sintered bodies, S0, S27, S52, S68, S87 and S100.

Figure 3. (a) Work hardening coefficient, n and (b) Strength Coefficient, K of sintered bodies vs. sintered density of Fe-3 mass% Cu hybrid steel alloyed powder + 0.7 mass% C. Number for each datapoint indicates R_{Cu}.

Figure 4. Optical microscopic images of the sintered specimens: (a) S0, (b) S27, (c) S52, (d) S68, (e) S87, and (f) S100, where d shows average grain diameter.

Figure 5. Dimensional changes vs. pre-alloyed Cu ratio in the Fe-3 mass% Cu hybrid steel alloyed powder.

Figure 6. Maps of Cu distribution obtained by EMPA for the sintered specimens: (a) S0, (b) S27, (c) S52, (d) S68, (e) S87, and (f) S100. White profile in each map illustrates the Cu concentration along the white line.

Figure 7. Average Cu concentrations of Cu-rich Cu-dilute areas estimated from the line analyses of Cu concentration shown in Figs.6(a)-6(f).

Figure 8. Comparison between the map of Cu distribution (left) and the optical micrograph (right) of S68 in the same field of view.

Figure 9. Nano-sized precipitates in ferrite phase surrounding pearlite phase, observed in specimen S68.

Colour figure (online version only)

Click here to access/download;Colour figure (online version only);Figure_2.tiff

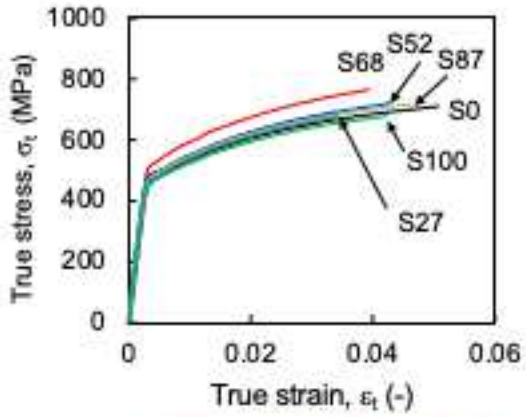

Fig. 2. True stress-true strain curves of the sintered bodies, S0, S27, S52, S68, S87 and S100.

Colour figure (online version only)

Click here to access/download;Colour figure (online version only);Figure_6.tiff

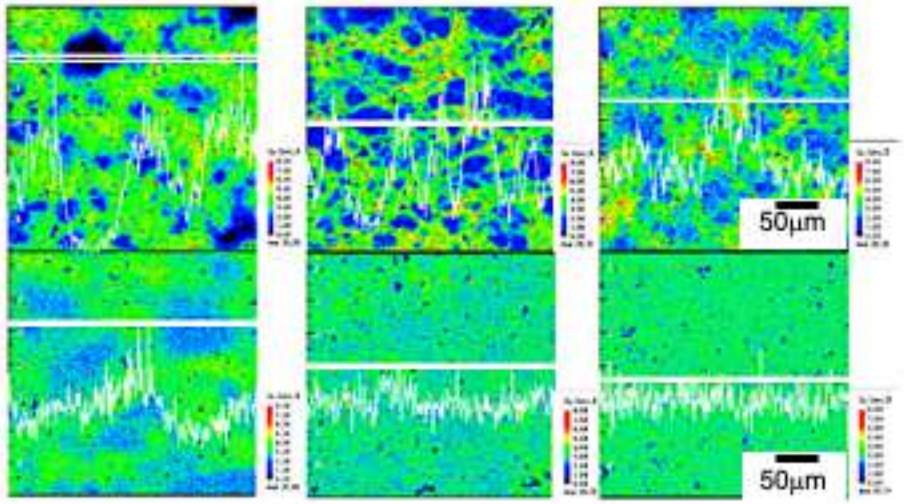

Fig.6 Maps of Cu distribution obtained by EMPA for the sintered specimens : (a) S0, (b) S27, (c) S52, (d) S68, (e) S87 and (f) S100. White spectrum in each map means Cu concentration along the white line.

Colour figure (online version only)

Click here to access/download;Colour figure (online version only);Figure_8.tiff

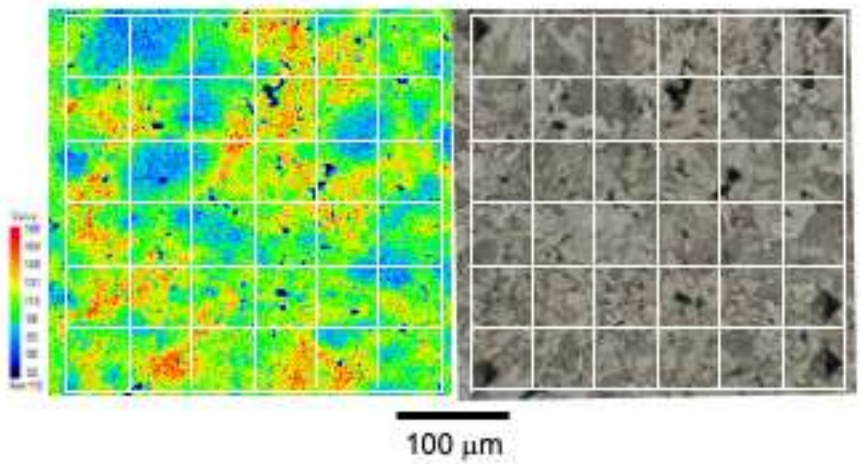

Fig. 8. Comparison between the map of Cu distribution (left) and the optical micrograph (right) of S68 in the same field of view.

Non-colour figure
Click here to access/download;Non-colour figure;Figure_1.tiff

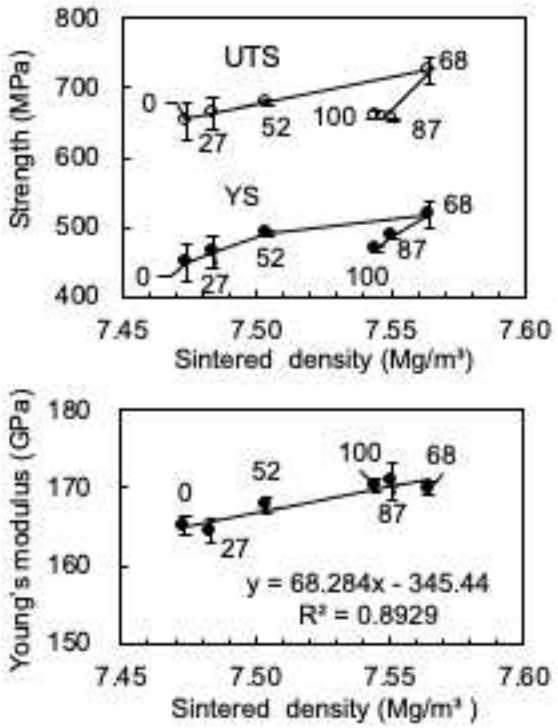

Fig. 1. (a) Strength and (b) Young's modulus vs. sintered density of Fe-3 mass% Cu hybrid steel alloyed powder + 0.7 mass% C. Number for each datapoint indicates R_{Cu}.

Non-colour figure

Click here to access/download;Non-colour figure;Figure_3.tiff

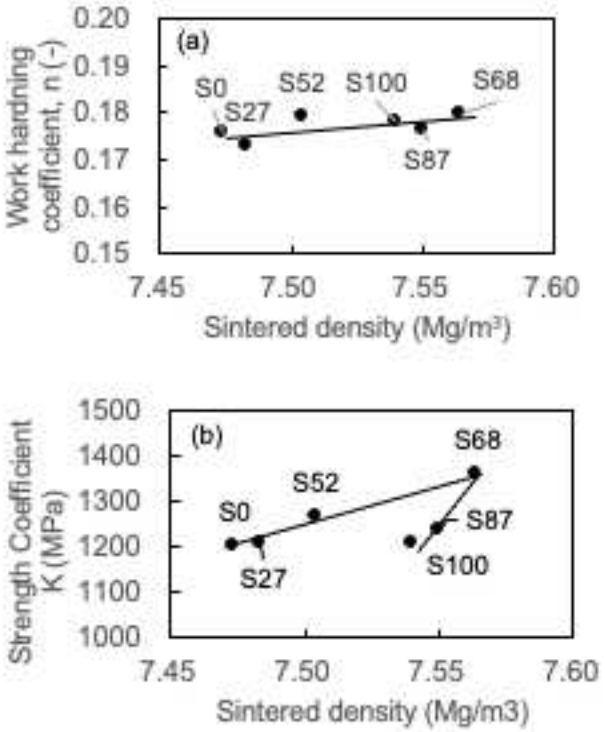

Fig. 3. (a) Work hardening coefficient, n and (b) Strength Coefficient, K of sintered bodies vs. sintered density of Fe-3 mass% Cu hybrid steel alloyed powder + 0.7 mass% C. Number for each datapoint indicates R_{Cu}.

Non-colour figure

Click here to access/download;Non-colour figure;Figure_4.tiff

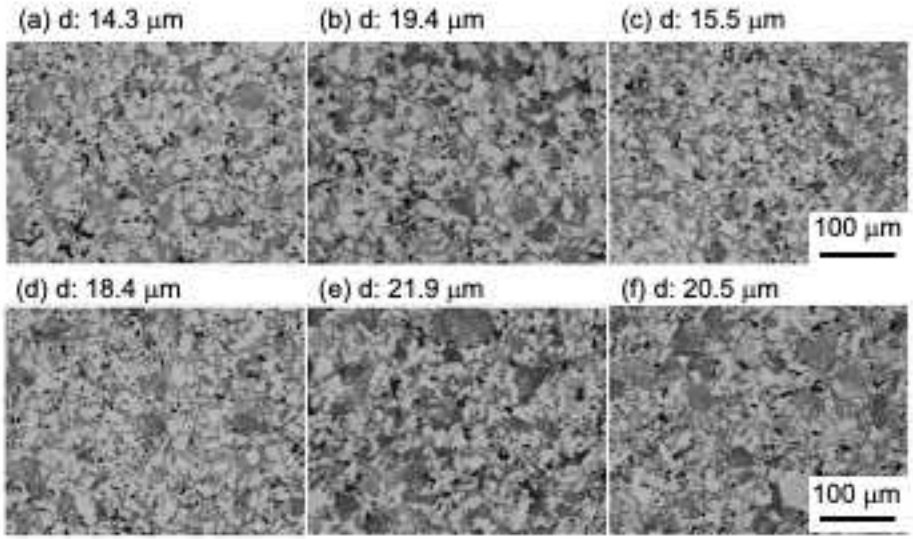

Fig. 4. Optical microscopic images of the sintered specimens: (a) S0, (b) S27, (c) S52, (d) S68, (e) S87, and (f) S100, where d shows average grain diameter.

Non-colour figure
Click here to access/download;Non-colour figure;Figure_5.tiff

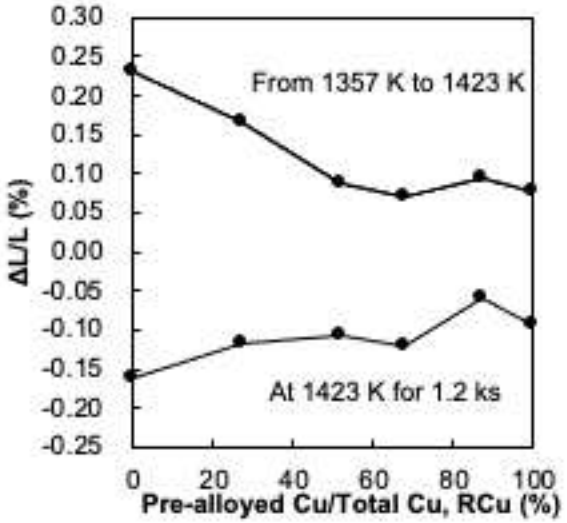

Fig. 5. Dimensional changes vs. pre-alloyed Cu ratio in the Fe-3 mass% Cu hybrid steel alloyed powder.

Non-colour figure

Click here to access/download;Non-colour figure;Figure_7.tiff

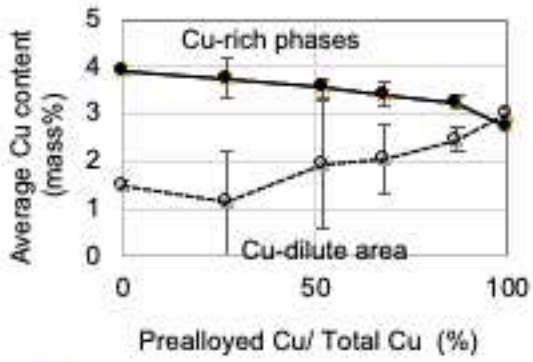

Fig.7 Average Cu concentrations of Cu-rich Cu-dilute areas estimated from the line analyses of Cu concentration shown in Figs.6(a)-6(f).

Non-colour figure
Click here to access/download;Non-colour figure;Figure_9.tiff

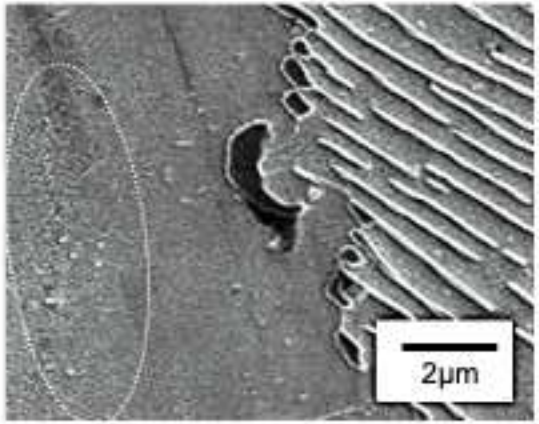

Fig. 9. Nano-sized precipitates in ferrite phase surrounding pearlite phase, observed in specimen S68.